Reaction Kinetics, Mechanisms and Catalysis (2024) 137:2363–2374
https://doi.org/10.1007/s11144-024-02627-9

Tungsten-doped MoS_2-based nanostructure for photocatalytic hydrogen evolution under visible light

Khursheed Ahmad[1] · Waseem Raza[2] · Mohd Quasim Khan[3] · Rais Ahmad Khan[4]

Received: 18 February 2024 / Accepted: 2 April 2024 / Published online: 2 May 2024

Abstract

In this work, we introduced a simple approach to boost the photocatalytic activity of MoS_2 by introducing transition metal (W) doping. The W-MoS_2 (10 mg) exhibited a substantial enhancement in photocatalytic activity for H_2 production, achieving an impressive rate of approximately 925 μmol g^{-1} after 6 h, which is 1.5-fold higher than bare MoS_2. The highest H_2 production activity of 1740 μmol g^{-1} after 6 h was obtained for 50 mg W-MoS_2 photocatalyst. The observed increase in activity can be ascribed to the formation of a Schottky barrier at the heterojunction interface, along with advantageous properties of improved active sites resulting from tungsten doping into MoS_2. Furthermore, the enhanced activity of W-MoS_2 may be attributed to the promotion of catalytic kinetics by tungsten and molybdenum sites, exhibiting commendable activity for water dissociation and higher efficiency in H^+ adsorption. These factors contribute significantly to the overall improved performance of the W-MoS_2 photocatalyst. Further, platinum (Pt) was also used as cocatalyst and enhanced photocatalytic activity of 2145 μmol g^{-1} after 6 h was observed for W-MoS_2 + 5 wt% Pt.

Keywords Tungsten doped MoS_2 · Photocatalytic system · Hydrogen evolution

✉ Mohd Quasim Khan
quasimkhanmohd90@gmail.com

[1] School of Materials Science and Engineering, Yeungnam University, Gyeongsan 38541, Republic of Korea

[2] Department of Materials Science and Engineering, WW4-LKO, University of Erlangen-Nuremberg, Martensstrasse 7, 91058 Erlangen, Germany

[3] Department of Chemistry, M.M.D.C, M.J.P. Rohilkhand University, Moradabad, Bareilly, Uttar Pradesh 244001, India

[4] Department of Chemistry, College of Science, King Saud University, 11451 Riyadh, Saudi Arabia

Introduction

Currently, society is facing two pivotal challenges: the energy crisis and environmental pollution [1, 2]. The predominant use of fossil fuels to fulfill the growing global energy demand not only contributes to environmental pollution but also poses the risk of irreversible anthropogenic climate change [3, 4]. Over recent years, photocatalytic hydrogen (H_2) production through the splitting of water has emerged as a viable and sustainable energy alternative to address future energy demand and manage environmental pollution [5–8]. Visible light-activated photocatalysts have attracted significant attention due to their capacity to harness the renewable and abundant energy inherent in solar radiation, presenting a clean and cost-effective solution. Consequently, the development of an efficient visible light-driven photocatalyst is deemed the "Holy Grail of material chemistry" representing a crucial element for the successful implementation of the photocatalytic process [9]. The interaction of light with a semiconductor photocatalyst is the heart of photocatalysis [9]. The photocatalysis process involves the generation of photo-induced charge carriers within the semiconductor photocatalyst in response to the absorption of suitable light, which then initiates the oxidation and reduction reactions [9]. The excited electrons in conduction from the valance band then react with H_2O or H^+ species in the aqueous environment to generate the desired H_2 [9]. Therefore, photocatalysis is based on three pivotal phases: light absorption, the generation and separation of charge carriers, and catalytic reactions [5]. The equilibrium between the thermodynamics and kinetics of these three crucial reaction steps is widely recognized as the main factor determining the overall efficiency of a photocatalytic system [5, 9]. Consequently, researchers have been making significant efforts to develop innovative photocatalysts that have better light absorption, effective separation of charge carriers, and efficient catalytic activity. From this perspective, metal chalcogenides have garnered significant attention, primarily due to their narrow band gap, rendering them effective photocatalysts for visible light activity [10]. Their attractiveness is further heightened by their expansive surface area, controllable morphology, and tunable band gap [11]. Furthermore, their optical and electric characteristics can be modified by fine-tuning both size and morphology [12].

Within the realm of chalcogenides, two-dimensional (2D) molybdenum disulfide (MoS_2) has emerged as a focal point for researchers in the field of material science. This is attributed to its remarkable features, including potent oxidizing activity, non-toxicity, high stability, a substantial surface area, and a notable abundance of catalytically active sites [13]. MoS_2 adopts a sandwiched structure with a hexagonal arrangement of Mo and S atoms (S–Mo–S), held together by van der Waals force. The exfoliation process of MoS_2 into a single or few layers of nanosheets shares similarities with graphene [13, 14]. MoS_2 possesses an indirect band gap of 1.29 eV, which can be readily converted into a direct band gap of 1.80 eV when transitioning from bulk material to thin layer [14]. This property allows MoS_2 to generate electron/hole pairs (e/h^+) upon exposure to visible light, making it a robust candidate for visible-light-induced photocatalyst for H_2

production through water splitting [14]. While MoS_2 is considered a strong candidate for visible-light-induced photocatalyst, it encounters a notable challenge. The limited ability to effectively separate and transfer photogenerated charge carriers to active sites is a common drawback [10]. This issue is characterized by a high rate of recombination efficiency of e/h^+ pairs due to short carrier lifetimes [15]. Additionally, the formation of Mo-S–O links during photocatalysis poses a constraint, restricting its broader application in the photocatalytic process [14]. To address these challenges, various strategies have been employed. These include morphological modifications, metal doping, and coupled with other semiconductors [15]. The introduction of metal doping, specifically, plays a crucial role in shifting the absorption of MoS_2, into the near-infrared range. [11, 15]. This process introduces defects that contribute to enhancing charge separation and interfacial charge transfer, along with a local electric field through the formation of Schottky junctions [15]. Meat-doping collectively aims to overcome the limitations associated with MoS_2 in photocatalysis [10, 14, 15]. The deposition of transition metals, particularly Cu, Ag, Pd, Au, and Pt has been explored as a method to create photocatalysts with enhanced visible light absorption [11, 15]. Additionally, the introduction of metallic heteroatoms into the MoS_2 lattice has been shown to effectively activate the basal plane S atoms and introduce in-plane active sites for the hydrogen evolution reaction (HER) [1]. Previous research has demonstrated that transition metals deposited on MoS_2 can serve as electron sinks, effectively capturing the photogenerated electron [15]. This mechanism accelerates the transfer and separation of e/h^+ pairs, showing the potential for improving the efficiency of the photocatalytic process. To date, various transition metal atoms, inducing Co [16], Ni [17] and Ru [18] have been successfully doped into MoS_2, demonstrating notably outstanding performance in the context of hydrogen evolution reaction. There has been a notable gap in prior research concerning the collaborative impact of defects within the MoS_2 lattice and the doping sites of tungsten atoms on the enhancement of H_2 generation. The introduction of W atoms induces lattice distortion in MoS_2, as the atomic radius of W is larger than that of Mo [19]. This distortion leads to the creation of additional defects, serving as active sites that contribute to a more effective H_2 generation process [19].

In this study, a simple and cost-effective one-step hydrothermal method was employed to synthesize the $W@MoS_2$ photocatalyst. The photocatalytic efficiency of H_2 generation was evaluated using various hole scavengers, revealing optimal performance in the presence of triethanolamine (TEOA). Remarkably, the $W@MoS_2$ photocatalyst demonstrated a substantial enhancement in photocatalytic activity for H_2 production, achieving an impressive rate of approximately 1740 μmol g^{-1} after 6 h. The notable increase in activity can be attributed to the formation of a Schottky barrier at the heterojunction interface, coupled with advantageous properties arising from tungsten doping into MoS_2. The synergistic activities of W doping and controlled MoS_2 surfaces effectively contribute to the separation of photo-generated charge carriers on the surface, enhancing electron transport to active regions for a more efficient photocatalytic process.

Experimental section

Materials and chemicals

We have purchased all the chemicals and reagents from Merck, Sigma and TCI and Fischer Scientific and used as received. All chemicals and reagents were of analytical grade.

Synthesis of W-MoS_2

Hydrothermal is well-known promising method to synthesize the metal oxides and metal sulfides with good reproducibility. In this work, hydrothermal method was used as synthetic technique for the synthesis of W-MoS_2. 0.45 g of ammonium molybdate was completely dissolved in 20 mL of the deionized water (DI water). 5 wt% of the tungsten source (tungsten chloride) was added to this prepared solution and stirred for few min at room temperature. In final step, 0.85 g of thiourea was added to the above solution and stirred for 20 min at RT. This reaction solution has been further transferred to the PTEE lined stainless steel autoclave and kept under oven and temperature of the oven was maintained 200 °C for 24 h. The W-MoS_2 sample was taken out from the autoclave by centrifuging the obtained solution and washed with ethanol and DI water. The W-MoS_2 was dried under vacuum oven at 60–70 °C for several h. The MoS_2 has been synthesized as discussed above except the addition of tungsten chloride.

Materials characterization

The synthesized samples i.e. MoS_2 and W-MoS_2 were characterized by powder X-ray diffraction (PXRD) method and PXRD patterns of the samples were analyzed on Empyrean Malvern Panalytical diffractometer with Cu K_α radiation ($\lambda = 1.54$ Å). The micro-morphological characteristics of the samples were analyzed on Zeiss Supra-55 field-emission electron microscope (FE-SEM) and energy dispersive X-ray spectroscopic (EDX) data has been obtained on Horiba EDX spectroscope. The photoluminescence (PL) spectrum of the samples were performed on Princeton Instruments Acton; SP2300. The X-ray photoelectron spectroscopic spectrum of the W-MoS_2 was obtained on Fischer-Scientific spectrometer.

Photocatalytic hydrogen evolution

25 mL of the lactic acid was added to the 75 mL of the DI water in quartz tube reactor. The synthesized W-MoS_2 (10 mg) has been added to the above prepared solvent mixture. The quartz tube was tightly closed and nitrogen gas was purged in to the above reactor to remove the oxygen and other gases. The light source for photocatalytic studied was a xenon lamp (300 W; wavelength = 420 nm). The different dose of the W-MoS_2 (10–70 mg) was used for optimization purposes. Platinum has been used as cocatalyst and different weight percentage of Pt (1, 2, 5 and 7%) was

used. The different hole scavenger agents such as methanol, ethanol, triethanolamine (TEOA), glycerol was used.

Results and discussion

Phase purity and crystal structure analysis

The phase purity and crystal structure of the synthesized pristine and W@MoS_2 photocatalysts were characterized through X-ray diffraction analysis, as illustrated in Fig. S1. The peaks observed at 14.1°, 34.6°, 41.3°, 51.02°, and 61.4° in the XRD spectra correspond to the hkl value of (002), (100), (103), (105) and (106). These peaks are consistently indexed to the hexagonal (2H-MoS_2) crystal structure, in accordance with standard data (JCPDS file No: 037–1492) [20]. It can be seen from fig s1 that there are no additional peaks associated with other phases. Due to minimal tungsten doping, no distinct peak corresponding to W is observed. However, a subtle shift towards lower angles in the characteristic peaks after tungsten doping suggests the successful incorporation of tungsten into MoS_2.

Surface morphology, EDX, and elemental mapping analysis

SEM analysis was employed to investigate the surface morphology of the prepared photocatalysts. As depicted in Figs. 1a and b, the SEM images illustrate the distinct features of both pristine and W@MoS_2 photocatalysts. The pristine MOS_2 exhibits three-dimensional (3D) flower-like nanoflakes, comprising multiple self-assembled thin nanosheets with remarkable uniformity (Fig. 1a). Similarly, the W@MoS_2 prepared with the same conditions exhibits a comparable 3D nanoflower morphology, characterized by ultrathin flakes with tungsten deposited on the surface of MoS_2 (Fig. 1b).

EDX analysis and mapping were performed to access the deposition of tungsten on the MoS_2 photocatalyst. Figs, S2 and S3a-S3d present the EDX and mapping results, revealing the presence of Mo, S, and W. The outcomes from EDX and elemental mapping collectively affirm the successful deposition of tungsten on MoS_2.

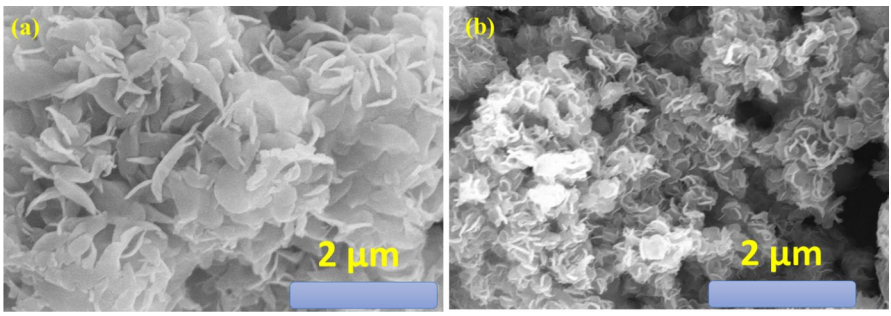

Fig. 1 SEM image of (**a**) the hydrothermally obtained (200 °C for 24 h) MoS_2 and (**b**) W-MoS_2

XPS analysis

X-ray photoelectron spectroscopy (XPS) analysis was conducted to explore the influence of W ions in MoS_2, elucidating the chemical composition, oxidation states, and bonding characterization of both pristine and W@MoS_2 photocatalysts. The high-resolution XPS spectrum of W 4f (Fig. S4a) reveals two prominent peaks at 35.2 ($4f_{7/2}$) and 37.4 eV ($4f_{5/2}$), with two weaker peaks at 34.1 ($4f_{7/2}$) and 36.4 eV ($4f_{5/2}$), inductive of W ions existing in two different valance states within W-MoS_2 (W^{4+} and W^{6+}) [21]. As depicted in Fig. S4b, the high-resolution XPS spectrum of Mo 3d displays three discernible peaks at 236.8, 233.2, and 229 eV, corresponding to Mo (IV)$3d_{3/2}$, Mo (IV)$3d_{5/2}$ and Mo (IV)$3d_{5/2}$ [13]. The high-resolution XPS spectra of S 2p of W@MoS_2 exhibit two characteristic peaks at 161.8 and 163.1 eV, attributed to energies of S $2p_{3/2}$ and S $2p_{1/2}$, respectively. These findings signify a -2 oxidation state in MoS_2, as shown in Fig. S3c [5, 8].

Optical properties and bad gap analysis

UV–vis Diffuse Reflectance Spectroscopy (UV-DRS) was employed to access the optical properties of both pristine and W-doped MoS_2, providing insight into the light-harvesting capabilities of synthesized photocatalysts [22]. In Fig. 2a, the UV-DRS spectra of pristine and W-doped MoS_2 photocatalysts reveal that the visible light harvesting ability of W-doped MoS_2 surpasses that of the pristine MoS_2. Band gap energies were determined using the formula $(\alpha h\upsilon)^2 = A\ (h\upsilon - E_g)$ for direct transitions. Figure 2b illustrates the relationship between $(\alpha h\upsilon)^2$ and $(h\upsilon)$, enabling the calculation of band energies. For pristine MoS_2, the calculated band gap energy is 1.9 eV. In contrast, the band gap energy for W-doped MoS_2 is slightly lower at 1.8 eV. This observation suggests that the introduction of W has significantly enhanced the absorption properties of MoS_2, signifying an improvement in the photo-catalyst's ability to harness light.

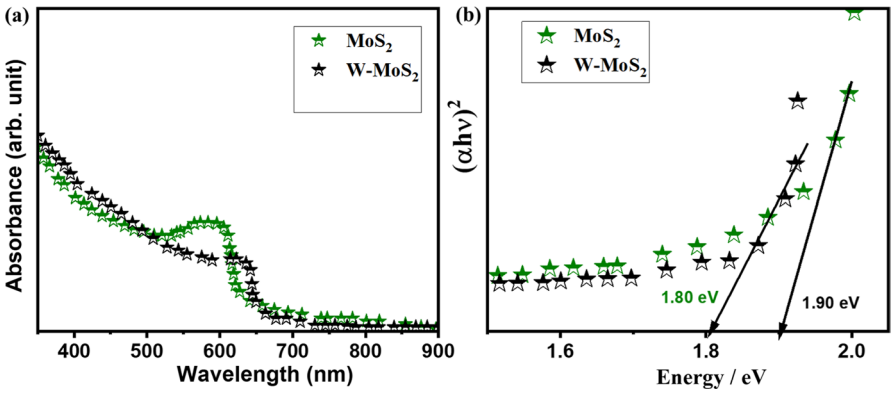

Fig. 2 **a** UV–vis spectrum and **b** Tauc plots of hydrothermally obtained MoS_2 and W-MoS_2

Photoluminescence (PL) analysis

Photoluminescence (PL) spectroscopy is a widely recognized and highly effective technique that has gained a lot of attention in the realm of photocatalysis for investigating the impact of doping/impurities [23]. This tool is used for comprehending recombination rate, trapping phenomena, migration dynamics, and electron transfer efficiencies within semiconducting materials. The observed PL intensity corresponds to a heightened recombination rate of e/h^+ pairs. In Fig. 3, the PL spectra of pristine and W-doped MoS_2 photocatalysts are depicted, revealing a noteworthy reduction in the PL intensity of MoS_2 after incorporation of W. This finding suggests that doping of W significantly impedes the recombination rate of photoinduced e/h^+ pairs in W-doped MoS_2 photocatalyst. As a result, it is expected that the photocatalytic activity of W-doped MoS_2 will exceed that of pristine MoS_2 photocatalyst.

Photocatalytic H_2 generation activities

The photocatalytic activity of both prepared pristine and W-doped MoS_2 was investigated through the splitting of water with lactic acid as a hole scavenger under visible light illumination (Fig. 4a). The H_2 production for W-doped MoS_2 (10 mg catalyst) was found to be 925 μmol g^{-1}, which is higher than pristine MoS_2 (575 μmol g^{-1}). These findings suggest that the introduction of W into MoS_2 accelerates the catalytic kinetics of the reaction, enhancing water dissociation activity and maintaining consistent hydrogen adsorption capability. Moreover, the doping of W into MoS_2 may create notable surface-active sites, leading to improved charge separation and transfer of photo-generated e^-/h^+ pairs, thereby improving photocatalytic activity. The photocatalytic H_2 production of W-doped MoS_2 was also evaluated in the presence of various hole scavengers under the same experimental conditions. Figure 4b presents the photocatalytic H_2 production with different hole scavengers in the presence of W-doped MoS_2 (10 mg). Notably, the highest H_2 evolution (1255 μmol g^{-1}) occurred in the presence of TEOA after 5 h, surpassing glycerol (705 μmol g^{-1}),

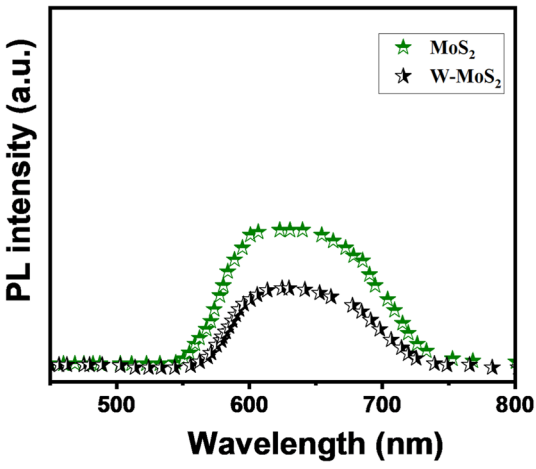

Fig. 3 PL spectra of hydrothermally obtained MoS_2 and W-MoS_2

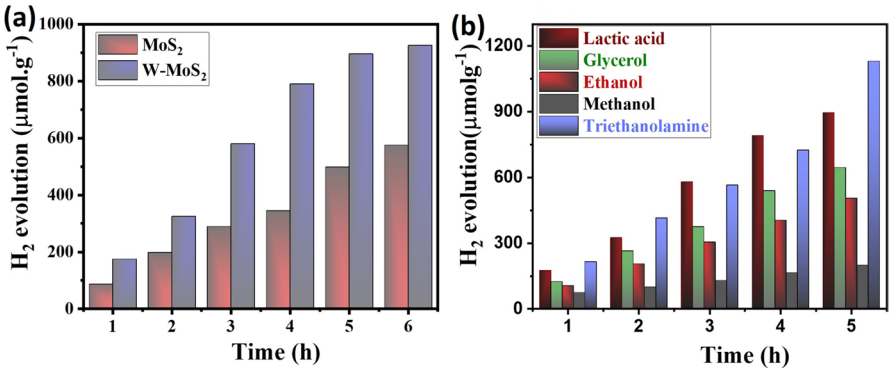

Fig. 4 **a** H_2 evolution activity of MoS_2 (10 mg catalyst) and W-MoS_2 (10 mg catalyst) in lactic acid. **b** H_2 evolution activity of W-MoS_2 (10 mg catalyst) in different hole scavengers (lactic acid, glycerol, ethanol, methanol, and triethanolamine)

ethanol (605 μmol g^{-1}), lactic acid (925 μmol g^{-1}), and methanol (245 μmol g^{-1}) and follows: TEOA > lactic acid > glycerol > ethanol > methanol (Fig. 4b). These results indicate the capability of the selected scavengers to trap the photo-generated holes from the valance band of the W-doped MoS_2 photocatalyst. This scavenging action prevents the recombination of holes with electrons, enabling the latter to actively contribute to H_2 production [24]. Additionally, the current doubling effect in different solvents may be attributed to the formation of unstable radicals, facilitating more efficient electron transfer from the hole scavenger to the conduction band of the photocatalyst [24, 25].

To investigate the activity of W-doped MoS_2 photocatalysts, control studies were conducted, especially focusing on optimizing the catalyst loading. In this context, experiments were performed to determine the optimal loading of the catalyst. The enhancement in the photocatalytic activity showed a parallel trend with the increase in the doses of W-doped MoS_2 photocatalyst, reaching an optimum at 50 mg of photocatalyst, after which a decline was observed (Figs. S5a and S5b). It could be seen from Figs. S5a and S5 that production of H_2 increases with the loading, possibly attributed to the availability of more surface-active sites [26]. The highest H_2 of 1740 μmol g^{-1} has been obtained for 50 mg catalyst (W-doped MoS_2), as shown in Fig. S5a. The H_2 production rate of 290 μmol h^{-1} g^{-1} has been observed for 50 mg catalyst (W-doped MoS_2), as depicted in Fig. S5b. However, beyond the optimal loading of 50 mg, there is a reduction in the activity of W-doped MoS_2 for H_2 production. This decrease is attributed to the agglomeration of photocatalysts, leading to a reduction in available surface area, diminished light penetration, and a decrease in active sites, consequently resulting in a reduction in H_2 production [27–29].

The W-MoS_2 photo-catalyst (50 mg) demonstrated good catalytic activity for H_2 generation but still need to be improved. The H_2 production can be further improved by utilizing cocatalysts. Platinum is well-known cocatalyst for H_2 production under visible light. In this context, we have further analyzed the photocatalytic activity of W-MoS_2 photo-catalyst (50 mg) with different weight percentage (1, 2, 5, and 7%)

of the Pt in presence of TEOA hole scavenger. The obtained results have been summarized in Fig. S5a. It is observed that H_2 production rate increases with increasing Pt percentage from 1 to 5% and highest H_2 amount of 2145 µmol g^{-1} was obtained for 5 wt% Pt (Fig. S5a). The reduced activity of H_2 production of 2084 µmol g^{-1} has been observed for 7 wt% Pt. The highest H_2 production rate of 357.5 $\mu mol.h^{-1}.g^{-1}$ was observed for 5 wt% Pt based photocatalytic systems (Fig. S5b).

In addition to achieving a high H_2 production, the long-term stability and reusability of photocatalysts are crucial considerations for their industrial application. The reusability and photostability of the W-doped MoS_2 were further investigated. Fig. S6a presents a slight deactivation in the photocatalyst's activity after four consecutive cycles, suggesting good stability over repeated use. The stability of the 5 wt% Pt was also checked and obtained results also demonstrated good stability for four consecutive cycles (Fig. S6b).

Finally, based on both experimental results and a comprehensive literature survey, we have established a probable reaction mechanism to elucidate the enhanced H_2 production observed in the W-doped MoS_2 photocatalyst (Fig. S6c).

In our study, TEOA serves as a hole scavenger, and visible light is employed to stimulate charge carriers for photocatalytic water-splitting experiments. A graphical representation of the charge transfer pathway for W-MoS_2 in the presence of Pt as co-catalysts under visible-light irradiation is shown in Fig. S4c. The positions of the conduction band (CB) and valence band (VB) of W-MoS2 were calculated using empirical Eqs. (1) and (2), informed by both experimental findings and relevant literature. [30–32]

$$E_{CB} = \chi - E^0 - 0.5\,E_{BG} \tag{1}$$

$$E_{VB} = E_{CB} + E_{BG} \tag{2}$$

Here E_{VB} and E_{CB} represent the VB and CB edges positions, χ is the absolute electronegativity of the W-MoS_2 (5.32 eV). E^0 is the free electron energy of the normal hydrogen electrode (NHE), which is 4.5 eV. Additionally, E_{BG} is represents the band gap energy of the W-MoS_2, calculated from the UV-DRS measurements using Tauc plot with MoS_2, s band gap estimated to be 1.8 eV. The corresponding values of E_{VB} and E_{CB} of W-MoS_2 are calculated to be − 0.08 eV and + 1.72 eV, respectively, with respect to NHE. Upon exposure to light, electrons are excited from the valance band (VB) to the conduction band (CB) of W-MoS_2, creating holes in the VB. These excited electrons are then effectively trapped by dopant (W), facilitating charge separation by mitigating the recombination rate. The Pt acted as cocatalyst and improved electron transportation. The trapped electrons will rapidly migrate to effectively reduce the captured oppositely charged H^+ ions, a pivot step in the efficient production of H_2. Simultaneously, the holes are scavenged by TEOA from VB of W-doped MoS_2 to oxide the sacrificial reagents ($TEOA^+$). This dual process leads to an extension of the lifetime of photo-induced charge carriers, ultimately resulting in an improvement in photocatalytic H_2 production.

The performance of the W-MoS_2 and W-MoS_2 + Pt (5 wt%) has been summarized in Table 1 which is comparable with reported literature.

Table 1 Comparison of H_2 evolution rate of W-MoS_2 and W-MoS_2 + Pt (5 wt%) with published articles

Photocatalysts	H_2 evolution rate ($\mu mol.h^{-1}.g^{-1}$)	Light source	Sacrificial agent	References
W-MoS_2	290	300 W; Xe lamp ($\lambda >= 420$ nm)	TEOA	This study
W-MoS_2 + Pt (5 wt%)	357.5	300 W; Xe lamp ($\lambda >= 420$ nm)	TEOA	This study
$ZnFe_2O_4/MoS_2$	142.1	300 W; Xe lamp ($\lambda >= 420$ nm)	Methanol	33
Phosphorus doped MoS_2	278.8	300 W; Xe lamp ($\lambda >= 420$ nm)	Na_2SO_3/ Na_2S	34
$Zn_{0.5}Cd_{0.5}S$	388.2	300 W; Xe lamp ($\lambda >= 420$ nm)	–	35
g-C_3N_4/MoS_2	84	300 W; Xe lamp ($\lambda >= 420$ nm)	TEOA	36
g-C_3N_4/Ag/MoS_2	208	300 W; Xe lamp ($\lambda >= 420$ nm)	TEOA	37
g-C_3N_4/MoS_2	133	300 W; Xe lamp ($\lambda >= 420$ nm)	TEOA	38
Bi_2O_3/MoS_2	10	300 W; Xe lamp ($\lambda >= 420$ nm)	Lactic acid	39

Conclusions

In summary, we successfully synthesized W-doped MoS_2 through a straightforward one-step hydrothermal method. Utilizing standard analytical techniques, we verified the uniform incorporation of W without inducing any change or damage to the material. The introduction of tungsten not only enhances the absorption of visible light by widening the band gap but also facilitates improved charge separation and transfer, resulting in elevated catalytic activity. Moreover, W-doped MoS_2 exhibits superior stability compared to pristine MoS_2, demonstrating remarkable photocatalytic H_2 production. The W doping significantly enhances the H_2 evolution rates, achieving approximately 1.5 times the rates compared to pristine MoS_2. The enhanced photocatalytic performance is attributed to extended light absorption, the creation of the Schottky barrier leading to more active sites, and suppression of charge recombination. Furthermore, the presence of a W dopant serves as an electron sink, ensuring ultrafast and efficient charge transportation for effective conversion of H^+ to H_2. Additionally, the doping of W in MoS_2 is anticipated to improve the catalytic kinetics of the reaction, as evidenced by its robust water dissociation activity and constant H_2 adsorption capability. The Pt has been employed as cocatalyst which further enhanced the hydrogen production rate.

Supplementary Information The online version contains supplementary material available at https://doi.org/10.1007/s11144-024-02627-9.

Acknowledgements R.A.K gratefully acknowledged Researchers Supporting Project (Project number, RSP2024R400), King Saud University, Riyadh, Saudi Arabia.

Data availability Authors elect to not to share data.

Declarations

Conflict of interests Authors declare no conflicts of interests.

References

1. Raza W, Ahmad K (2021) *Handb. Greener Synth. Nanomater. Compd.* Elsevier 917–938.
2. Raza W (2021) *All-Carbon Compos. Hybrids*, Royal Society Of Chem. 77–98.
3. Ahmad K, Raza W, Khan MQ (2021) *Handb. Greener Synth. Nanomater. Compd. Vol. 2 Synth. Macroscale Nanoscale*, Elsevier 549–564.
4. Raza W, Ahmad K (2021) *Handb. Greener Synth. Nanomater. Compd. Vol. 1 Fundam. Princ. Methods*, Elsevier 917–938.
5. Raza W, Tesler AB, Mazare A, Tomanec O, Kment S, Schmuki P (2023) ChemCatChem 15:e202300327
6. Zeng D, Li Y (2024) Appl Catal B Environ 342:123393
7. Li Y, Li S, Meng L, Peng S (2023) J Colloid Interf Sci 650:266–274
8. Raza W, Kerketta U, Hwang I, Schmuki P (2022) ChemElectroChem 9:e202200706
9. Raza W, Ahmad K, Khan RA, Kim H (2023) Int J Hydrogen Energy 48:29071
10. Li Y, Han P, Hou Y, Peng S, Kuang X (2019) Appl Catal B: Environ 244:604–611
11. Li Y, Hou Y, Fu Q, Peng S, Hu YH (2017) Appl Catal B: Environ 206:726–733
12. Li Y, Wang H, Peng S (2014) J Phys Chem C 118:19842–19848
13. Ahmad K, Raza W, Alsulmi A, Kim H (2023) Diam Relat Mater 138:110178
14. Riaz KN, Yousaf N, Tahir MB, Israr Z, Iqbal T (2019) Int J Energy Res 43:491
15. Rahman A, Jennings JR, Tan AL, Khan MM (2022) ACS Omega 7:22089
16. Dai X, Du K, Li Z, Liu M, Ma Y, Sun H, Zhang X, Yang Y (2015) ACS Appl Mater Interf 7:27242
17. Miao J, Xiao FX, Yang HB, Khoo SY, Chen J, Fan Z, Hsu YY, Chen HM, Zhang H, Liu B (2015). Adv Sci. https://doi.org/10.1126/sciadv.1500259)
18. Zhang J, Xu X, Yang L, Cheng D, Cao D (2019) Small Meth 3:1900653
19. Xu Q, Zhang Y, Zheng Y, Liu Y, Tian Z, Shi Y, Wang Z, Ma J, Zheng W (2021) J Phys Chem C 125:11369
20. Chen J, Xia Y, Yang J, Chen B (2018) Appl Phys A Mater Sci Process 124:1
21. Chen R, Pei Y, Kang Y, Liu J, Xia Y, Wang J, Xu H, Jiang C, Li W, Xiao X (2022) Adv Electron Mater 8:2200281
22. Raza W, Faisal SM, Owais M, Bahnemann D, Muneer M (2016) RSC Adv 6:78335
23. Raza W, Bahnemann D, Muneer M (2018) Catal Today 300:89
24. Denisov N, Yoo JE, Schmuki P (2019) Electrochim Acta 319:61
25. Schlenkrich J, Lübkemann-Warwas F, Graf RT, Wesemann C, Schoske L, Rosebrock M, Hindricks KDJ, Behrens P, Bahnemann DW, Dorfs D, Bigall NC (2023) Small 19:2208108
26. Raza W, Bahnemann D, Muneer M (2017) J Photochem Photobiol A Chem 342:102
27. Raza W, Khan A, Alam U, Muneer M, Bahnemann D (2016) J Mol Struct 1107:39
28. Raza W, Haque MM, Muneer M, Harada T, Matsumura M (2015) J Alloys Compd 648:641
29. Raza W, Haque MM, Muneer M (2014) Appl Surf Sci 322:215
30. Osuagwu B, Raza W, Tesler AB, Schmuki P (2021) Nanoscale 13:12750–12756
31. Zheng Z, Yu L, Gao M et al (2020) Nat Commun 11:3315
32. Barpuzary D, Banik A, Gogoia G, Qureshi M (2015) J Mater Chem A 3:14378–14388
33. Nagajyothi PC, Devarayapalli KC, Shim J, Prabhakar Vattikuti SV (2020) Int J Hydrogen Energy 45:32756–32769
34. Xin X, Song Y, Guo S, Zhang Y, Wang B, Wang Y, Li X (2020) J Alloys Comp 829:154635
35. Zhang Y, Lu D, Li H, Kondamareddy KK, Wang H, Zhang B, Wang J, Wu Q, Zeng Y, Zhang X, Zhou M, Neena D, Hao H, Pei H, Fan H (2022) Appl Surf Sci 586:152770

36. Shi X, Fujitsuka M, Kim S, Majima T (2018) Small 14:1703277
37. Lu D, Wang H, Zhao X, Kondamareddy KK, Ding J, Li C, Fang P (2017) ACS Sustain Chem Eng 5:1436–1445
38. Liu Y, Zhang H, Ke J, Zhang J, Tian W, Xu X, Duan X, Sun H, Tade MO, Wang S (2018) Appl Catal B Environ 228:64–74
39. Khalid NR, Israr Z, Tahir MB, Iqbal T (2020) Int J Hydrogen Energy 45:8479–8489